PHYSICAL REVIEW MATERIALS **6**, 083802 (2022)

Generalized design principles for hydrodynamic electron transport in anisotropic metals

Yaxian Wang,[1,*] Georgios Varnavides,[1,2,3,*] Ravishankar Sundararaman,[4] Polina Anikeeva,[2,3]
Johannes Gooth,[5] Claudia Felser,[5] and Prineha Narang[1,†]
[1]*John A. Paulson School of Engineering and Applied Sciences, Harvard University, Cambridge, Massachusetts 02138, USA*
[2]*Department of Materials Science and Engineering, Massachusetts Institute of Technology, Cambridge, Massachusetts 02139, USA*
[3]*Research Laboratory of Electronics, Massachusetts Institute of Technology, Cambridge, Massachusetts 02139, USA*
[4]*Department of Materials Science and Engineering, Rensselaer Polytechnic Institute, Troy, New York 12180, USA*
[5]*Max Planck Institute for Chemical Physics of Solids, Nöthnitzer Strasse 40, 01187 Dresden, Germany*

(Received 18 November 2021; revised 26 April 2022; accepted 23 June 2022; published 12 August 2022)

Interactions of charge carriers with lattice vibrations, or phonons, play a critical role in unconventional electronic transport of metals and semimetals. Recent observations of phonon-mediated collective electron flow in bulk semimetals, termed electron hydrodynamics, present new opportunities in the search for strong electron-electron interactions in high carrier density materials. Here we present the general transport signatures of such a second-order scattering mechanism, along with analytical limits at the Eliashberg level of theory. We study electronic transport, using *ab initio* calculations, in finite-size channels of semimetallic ZrSiS and $TaAs_2$ with and without topological band crossings, respectively. The order of magnitude separation between momentum-relaxing and momentum-conserving scattering length scales across a wide temperature range make both of them promising candidates for further experimental observation of electron hydrodynamics. More generally, our calculations suggest that the hydrodynamic transport regime does not, to first order, rely on the topological nature of the bands. Finally, we discuss general design principles guiding future search for hydrodynamic candidates, based on the analytical formulation and our *ab initio* predictions. We find that systems with strong electron-phonon interactions, reduced electronic phase space, and suppressed phonon-phonon scattering at temperatures of interest are likely to feature hydrodynamic electron transport. We predict that layered and/or anisotropic semimetals composed of half-filled d shells and light group V/VI elements with lower crystal symmetry are promising candidates to observe hydrodynamic phenomena in the future.

DOI: 10.1103/PhysRevMaterials.6.083802

I. INTRODUCTION

Hydrodynamic electron transport, where charge carriers can flow collectively akin to a classical fluid, has recently garnered significant attention as a probe of strong electron interactions in conductors, with increasing technological relevance as electronic devices approach the micro- and nanometer scale. For instance, in a hydrodynamic conductor resistive processes occur predominantly at the boundaries, which alters the spatial distribution of joule heating and can thereby significantly impact thermal design. Further, it has been demonstrated that, in a narrow conducting channel, collective flow can transfer charge more efficiently than the ballistic regime, thus achieving "superballistic" transport [1]. Microscopically, this requires that the total momentum of electrons is conserved, with the momentum-relaxing interactions of electrons with impurities, lattice vibrations, or the device boundary being significantly slower. The hydrodynamic transport regime has until recently been inaccessible since at high temperatures the electron momentum is often relaxed by lattice vibrations, while at low temperatures by extrinsic scattering due to high impurity concentrations. In these systems charge transport is governed by diffusive processes, where the electrons lose their momentum after traveling an average "mean free path" distance (l_{mr}).

To observe hydrodynamic effects, the momentum conserving length scale (l_{mc}) needs to dominate, necessitating electron-electron scattering to be frequent enough. Since the strength of conventional Coulomb interactions depends inversely on the carrier density [2], hydrodynamic transport is most likely to occur in semiconductors or low carrier-density semimetals such as graphene. This is supported by the first observations of hydrodynamic electron flow in two dimensional electron gases (2DEG) (Al,Ga)As [3], and more recently graphene [4–6]. However, potential applications and optimization of this transport regime are hindered because in semiconductors sufficiently high carrier concentrations are usually achieved by impurities, which in turn dominate the scattering at low temperatures, while in bulk metals with high carrier densities conventional Coulomb interactions are screened.

The growth of high quality single crystals with very low levels of impurities has facilitated recent observations of hydrodynamic transport in a handful of high carrier-density systems such as semimetals WP_2 [7] and WTe_2 [8], and delafossite metals $PdCoO_2$ and $PtCoO_2$ [9,10], where the

---

[*] These authors contributed equally to this work.
[†] prineha@seas.harvard.edu

observation could not readily be explained using the Coulomb interaction [8,11]. Instead, a combination of theory and experiment shows an indirect electron-electron interaction, mediated by an intermediate phonon, dominates at moderate temperatures [8,11]. This provides an opportunity to realize and optimize hydrodynamic effects in a broader family of materials, ideally with high carrier mobility and tunable sample quality. Despite these theoretical advances in understanding the macroscopic observables of hydrodynamic phenomena [3,12,13], general design principles guiding the discovery of bulk hydrodynamic candidates remain elusive.

In this article, we explore the phonon-mediated electron-electron scattering mechanism in anisotropic metals and semimetals with *ab initio* calculations. We investigate the possibility of hydrodynamic electron flow in semimetals ZrSiS and $TaAs_2$, the former of which has three-dimensional Dirac nodal lines while the latter has no Dirac or Weyl crossings. We find that both materials host strong phonon-mediated electron-electron interactions and are promising candidates to exhibit hydrodynamic behavior at relatively higher cryogenic temperatures than previously reported systems. Inspired by the recent development of temperature-dependent imaging techniques that can spatially resolve the electron current profile via nitrogen-vacancy magnetometry [8,14,15], we compute the current density profiles for various combinations of momentum relaxing and momentum conserving length scales, and characterize the resulting transport regimes at different temperatures to provide guidance for experimentally relevant hydrodynamic observables.

Further, in this article we investigate the analytical limits of the phonon-mediated scattering lifetime, and provide empirical evidence to support these limits in light of this work and previously explored semimetals [8,16,17]. At temperatures significantly lower than the system's Debye temperature, when anharmonic phonon-phonon interactions are significantly slower than electron-phonon interactions, resulting in long-lived phonon excitations which preferentially transfer their momenta to the electronic system, the second-order phonon-mediated electron lifetime is shorter than the first-order electron-phonon lifetime. This effectively shifts the focus in the search for hydrodynamic candidates to ultrapure materials with long momentum-relaxing mean free paths, significantly expanding the pool for future search. Finally, we discuss the essential features leading to hydrodynamic electron transport in metallic candidates: (a) strong electron-phonon coupling, typically found in low-symmetry crystals composed of d/p orbitals [18]; (b) suppressed phonon-phonon interactions, e.g., realized through the "acoustic bunching" effect in systems with relatively large atomic mass difference [19]; (c) high Fermi velocity often correlated with highly dispersive electronic bands as well as low levels of disorder. Additionally, we note that electron-electron Umklapp scattering, which effectively relaxes the total electron quasimomentum leading to contributions to the electrical resistivity at low temperatures [20], also needs to be minimized. From these predictions and observations we conclude that anisotropic quantum materials composed of transition metals and group V/VI elements host multiple materials families suitable for exhibiting and optimizing hydrodynamic electron flow.

II. OVERVIEW OF MATERIAL PROPERTIES IN PHONON-MEDIATED HYDRODYNAMIC CANDIDATES

At first glance, the observation of hydrodynamic electron transport in three dimensional bulk conductors appears serendipitous in nature, since conventional electron-electron Coulomb interactions are expected to be short ranged due to electron screening effects. More specifically, recent temperature- and spatially resolved measurements on WTe_2 show evidence of nonuniform flow at ~20 K [8]. Meanwhile, bulk transport signatures on WP_2 feature strong deviations from the Wiedemann-Franz law [7], while the temperature dependence of phonon linewidths in WP_2 cannot be readily explained via lattice anharmonicity models and provides evidence of strong phonon-electron coupling [17]. Similarly, the width-dependent resistivity in narrow conducting channels of $PdCoO_2$ indicated a $l_{\mathrm{mc}}/l_{\mathrm{mr}} \sim 0.1$ ratio meaning momentum-conserving mean free paths are as short as a few microns [10], in contrast to conventional electron-electron interactions from the Fermi-liquid theory estimating l_{mc} on the order of thousands of microns [21]. In a series of recent theoretical predictions, phonon-mediated electron-electron scattering is shown to be important for the nondiffusive electron transport in these systems [7,8,11,16,17]. Since momentum-relaxing scattering needs to be minimized to observe hydrodynamic effects, it is important for material candidates to exhibit long momentum-relaxing l_{mr}. In this section we examine the metals and semimetals WP_2, WTe_2, and $PdCoO_2$ that exhibit signatures of hydrodynamics and the material properties that enable this physics.

Intuitively, delocalized electrons, for example from s orbitals, usually lead to large dispersion in band energy, that is, larger Fermi velocity, v_F. However, they typically result in symmetric bonding states often found in isotropic lattices, making them less sensitive to lattice vibrations. To access the second-order phonon-mediated interactions, we seek strong electron-phonon coupling across the Fermi surface (see Sec. IV); therefore, more localized electrons, for example, hybridized d orbitals, are advantageous. By contrast, suppression of the first-order momentum-relaxing scattering can be achieved in a number of ways [22,23] (each individually effective though a confluence would be beneficial). (I) In semimetals with well separated electron/hole Fermi pockets across the Brillouin zone. Crystals with lower symmetry and complex orbital hybridization usually have their conduction band minimum and valance band maximum shifted from the zone center, so their Fermi surfaces are located away from each other. Here, at low temperatures, phonon excitations lack the momentum to couple electrons from one pocket to another, and only intraband scattering is allowed [Figs. 1(a) and 1(b)]. (II) At low temperatures where the phonon phase space is significantly reduced, momentum-relaxing scattering is ineffective at relaxing the system's momentum appreciably [Fig. 1(c)], while momentum-conserving electron-electron scattering via the "instantaneous" emission and reabsorption of phonon modes [Fig. 1(d)] is allowed to take place for larger $\boldsymbol{q}$. (III) On Fermi surfaces with nontrivial geometry where the small scattering efficiency factor leads to "quasi" conservation of electron momentum [Fig. 1(e)]. Specifically, at very low temperatures, small phonon momenta $\boldsymbol{q}$ always result in a

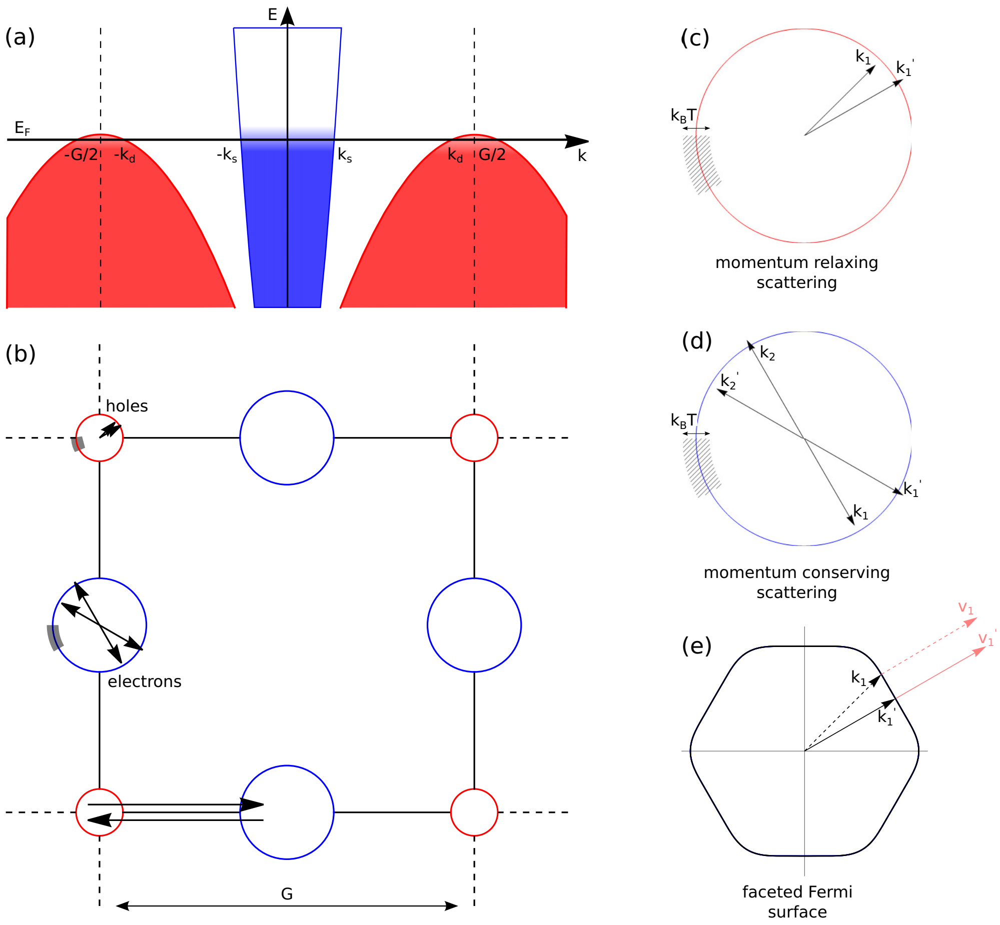

FIG. 1. (a) Schematic energy dispersion diagram along a high symmetry direction for a semimetal, with highly dispersive s/p electronlike (blue) and "heavy" d/f holelike (red) bands crossing the Fermi energy. Due to the separation of the Fermi pockets, lattice excitations with a large wave number are needed for transition between k_s and k_d. (b) Fermi surface diagram of the semimetal shown in (a) across the first Brillouin zone, showing intrapocket (top left) and interpocket (bottom) scattering events. The square lattice Brillouin zone, with reciprocal lattice vector G, is shown in solid lines. Adapted from Ref. [22]. (c) Electron-phonon momentum relaxing scattering event, where initial electronic state $\boldsymbol{k}$ is scattered into final state $\boldsymbol{k}'$, exchanging both energy and momentum to the phonon mode $\boldsymbol{q} = \boldsymbol{k}' - \boldsymbol{k}$. The thermally accessible states with energy $\sim k_B T$ around the Fermi energy are indicated by the shaded area. (d) Electron-electron momentum conserving scattering event, where two initial electronic states $\boldsymbol{k_1}$ and $\boldsymbol{k_2}$ are scattered into final states $\boldsymbol{k}_1'$ and $\boldsymbol{k}_2'$. The scattering process conserves both energy and momentum. (e) A faceted Fermi surface, on which a scattering event between wave vectors from $\boldsymbol{k}$ to $\boldsymbol{k}'$ may lead to negligible change in the electron velocity such that the total momentum stays "quasi" conserved.

small angle between the incident, $\boldsymbol{k}$, and scattered electron momentum, $\boldsymbol{k}' = \boldsymbol{k} - \boldsymbol{q}$. On a Fermi surface with nontrivial geometry, the electron velocity v_F can deviate significantly from the wave vector and thus affect the transport-relevant scattering efficiency [11,24]. We can quantify this effect by taking into account the scattering angle after scattering [16,24]:

$$1 - \cos\theta = 1 - \frac{\mathrm{v}_{n\boldsymbol{k}} \cdot \mathrm{v}_{m\boldsymbol{k+q}}}{|\mathrm{v}_{n\boldsymbol{k}}||\mathrm{v}_{m\boldsymbol{k+q}}|}. \tag{1}$$

One such example is shown in Fig. 1(e), when the concave portions of the Fermi surface result in a strong velocity and mean free path distribution anisotropy [25,26], and can further reduce the momentum relaxing scattering efficiency.

Recent first principles calculations have provided significant insights into the state-resolved momentum relaxing lifetimes in these systems [8,11,16]. WP_2 [16] and WTe_2 [8] both show a similar trend in the carrier lifetime distribution on their Fermi surfaces. At high temperatures, the momentum relaxing lifetimes are distributed more evenly on electron/hole pockets compared to extremely low temperatures, where the long lived electrons are "focused" to specific spots on the hole pockets, which have open Fermi surface shape and thus reduced electronic phase space. For $PdCoO_2$, which has a faceted open Fermi surface in a hexagonal shape, at high temperatures, long-lived electrons span the entire Brillouin zone along both k_z and $k_{x/y}$ [11], while at 4 K, the long-lived electrons are located only at the corners of the hexagonal Fermi surface at $k_z = 0$. Taken together, the highly dispersive hole bands give rise to large Fermi velocity and smaller phase space for electron-phonon scattering. Yet, the strong electron-phonon coupling arising from d orbitals leads to a strong second-order electron-electron interaction mediated by a intermediate phonon. These emerging common features motivate us to search for hydrodynamic candidates in layered and/or anisotropic structures with transition

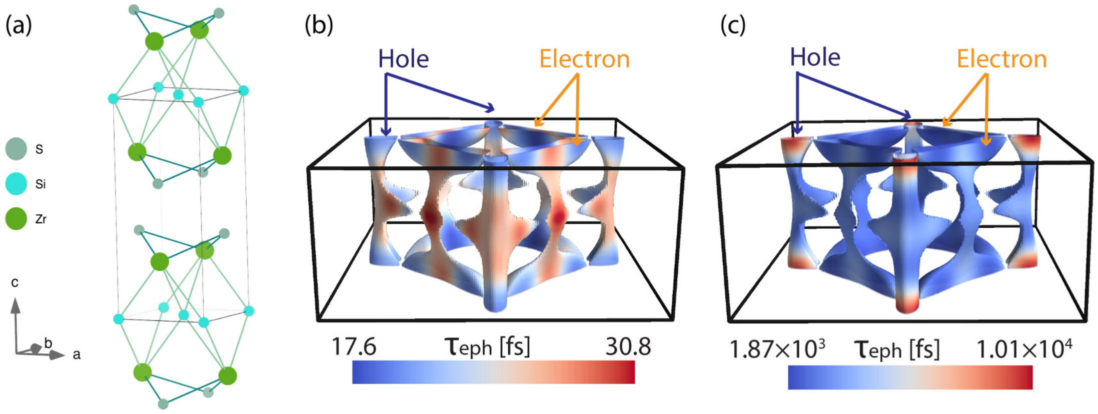

FIG. 2. (a) Crystal lattice of ZrSiS, highlighting the layered structure. (b),(c) Electron-phonon lifetimes (τ_{eph}) at (b) 298 K and (c) 4 K projected on the Fermi surface of ZrSiS. Similarly, while both electron and hole pockets have long lived carriers, lowering temperature quenches the scattering events on the hole pockets much more significantly.

metals and group V/VI elements, and to postulate generalized design principles. Meanwhile, various electronic transport signatures are indicative of the otherwise hard to experimentally obtain electron-phonon coupling strength. For example, large RRR (residual-resistivity ratio) is an important sign of low-impurity samples and large MR (magnetoresistance) can indicate charge compensation, unconventional Fermi surface topology, and scattering mechanisms.

III. *AB INITIO* PREDICTIONS OF ELECTRON HYDRODYNAMICS IN ANISOTROPIC METALS

Following the design principles discussed in Sec. II, we investigate layered compounds with transition metals that show unconventional transport signatures, more specifically MR. This is because, while hydrodynamic electron flow has only been experimentally reported in a few bulk systems, anomalous MR has been heavily studied in recent literature. Large positive (and mostly linear) MR has been found in many semimetals including but not limited to WTe_2 [27,28], LaBi [29], $NbIrTe_4$ [30], etc. In addition, large extremely anisotropic MR is reported in Dirac nodal line semimetal ZrSiS [31,32] and ZrSi(Se,Te) [33]. Further, negative MR was found in topological semimetals [34–36], a semimetal $TaAs_2$ without Dirac dispersion [37], and at the $LaAlO_3/SrTiO_3$ interface [38]. These observations suggest the pool of candidates for hydrodynamic electron flow in bulk materials may be much larger than previously thought. In this section we present calculations of ZrSiS and $TaAs_2$ as case studies to evaluate these design principles.

ZrSiS crystallizes in the PbFCl-type tetragonal $P4/nmm$ structure [Fig. 2(a)], and has been shown to host a three-dimensional Dirac line node and feature a chiral anomaly and extremely large nonsaturating MR [31,32,43–46]. Nonsaturating MR results from charge compensation of its high mobility carriers with a ratio of ~0.94 electrons to holes, similar to WTe_2. Moreover, the tube-shaped Fermi surface oriented along the crystallographic $\hat{c}$ direction leads to open electron orbits under magnetic fields, which can give rise to strong anisotropic MR [32,46]. These signatures indicate the possibility of hydrodynamic electron flow in this material that we investigate next.

Figures 2(b) and 2(c) show the Fermi surface of ZrSiS, composed of four degenerate electron and hole pockets due to the mirror symmetry in the *ab* plane all in open shape, in agreement with previous work [31,32,43,44]. The behavior of momentum-relaxing electron-phonon lifetimes (τ_{eph}; for details see Appendix C) at 298 K and 4 K shows substantial similarity with those in other systems mentioned above, such as WTe_2 and WP_2. While at 298 K longer-lived carriers appear evenly distributed between electron and hole pockets, at 4 K the only long-lived carriers are located on hole pockets at the zone boundary. Using the formalism developed in Sec. IV, the phonon-mediated electron-electron lifetime ($\tau_{\mathrm{ee(ph)}}$) is much shorter than the momentum relaxing electron-phonon lifetimes across all temperatures [Fig. 3(a)]. Therefore, the crossover between the dominant scattering mechanism is determined by the impurity scattering mean free path (l_{imp}). High quality ZrSiS samples have been shown to have an impurity mean free path $l_{\mathrm{imp}} > 1$ μm [39,47]. Using $l_{\mathrm{imp}} = 1$ μm, momentum relaxing events appear to dominate below ~20 K [Fig. 3(a)], allowing for the possibility of observing hydrodynamic flow at higher temperatures. Further, the expected current density (j_x) profiles with various combinations of l_{mc} and l_{mr} in a narrow conducting channel are computed from solving the spatially resolved Boltzmann transport equation (see Appendix D). The contour plot of the j_x curvature gives a general metric to characterize different transport regime limits. Using the l_{mc} and l_{mr} values obtained from *ab initio* calculations, we can bridge the microscopic scattering mechanisms with these observables and examine how strong the hydrodynamic effect is in samples with different dimensions [Fig. 3(b)]. Our results suggest hydrodynamic electron flow can be realized in narrow, submicron devices. Alternatively, if sample quality is further improved to $l_{\mathrm{imp}} \approx 5$ μm, the hydrodynamic window can be expanded to lower temperatures and wider devices. Compared to that of WTe_2, l_{mc} is relatively small in ZrSiS, due to a larger carrier concentration (~9×10^{19} cm^{-3} in ZrSiS [31] versus ~2×10^{19} cm^{-3} in WTe_2 [8]).

While hydrodynamic signatures in the topological semimetals we considered so far (ZrSiS, WP_2, and WTe_2) are similar, it is intriguing to address the necessity of topologically protected states in the context of hydrodynamic

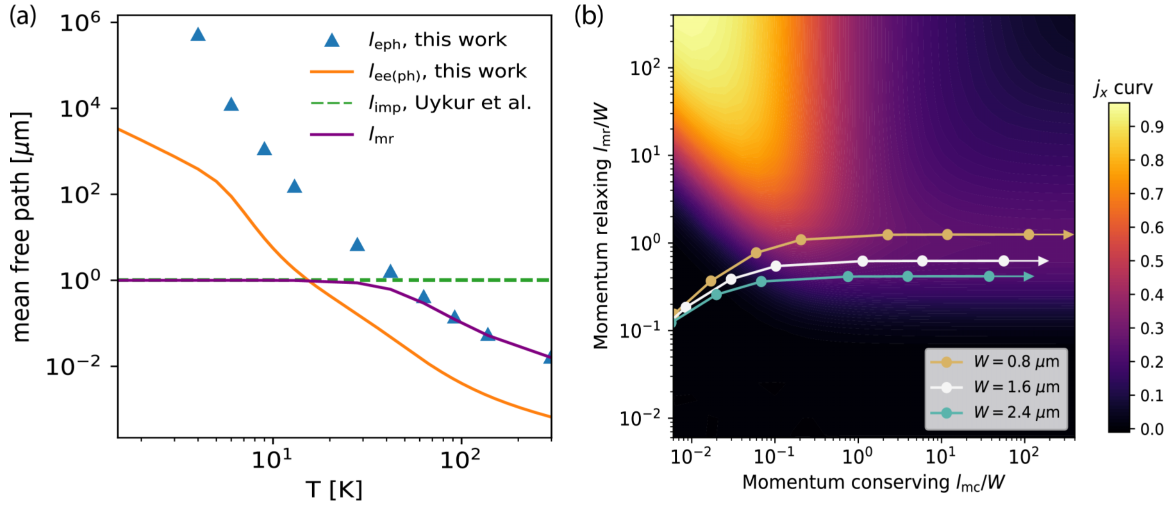

FIG. 3. (a) Temperature dependence of first-order electron-phonon (l_{eph}) and second-order phonon mediated electron-electron ($l_{\mathrm{ee(ph)}}$) mean free paths in ZrSiS calculated from *ab initio*. The impurity mean free path is taken as 1 μm from Uykur *et al.* [39]. Assuming that, at low temperatures, impurity scattering is the dominant electron resistivity mechanism, we estimate the impurity concentration to be 1.5×10^{15} cm^{-3} according to $\rho^{\mathrm{3D}}_{\mathrm{unitary}} = \frac{4\pi\hbar n_d}{ne^2k_F}$ [40–42]. (b) Normalized j_x curvature phase diagram. Overlaid lines show the trajectories with the decreasing temperature with different channel widths.

transport. The role of topology in Dirac-Weyl semimetals that exhibit signatures of hydrodynamics has sparked intense debates in the field. To address this open question, we turn to TaAs$_2$ as a case study for a semimetal without nontrivial band crossings. TaAs$_2$ crystallizes in the monoclinic $C12/m1$ structure with two chemical sites for As atoms, one forming Ta-As planes with Ta atoms and the other bridging the interlayer coupling [Fig. 4(a)]. As a nonmagnetic material, TaAs$_2$ has been shown to have giant MR from high mobility compensated charge carriers [37,48–51]. However, the band crossings are gapped in the presence of spin orbit coupling, making it an interesting case to study hydrodynamic behavior in topologically trivial semimetals. Owing to a small effective mass $m^* \sim 0.3m_0$ [48,50], the carrier mean free path is estimated to be $\sim$10 μm at 2 K, significantly longer than that of WTe$_2$ and ZrSiS. Moreover, in a high quality TaAs$_2$ crystal with carrier density $\approx 2.8 \times 10^{18}$ cm^{-3}, the MR is nearly one magnitude larger than that of WTe$_2$ [49], and the carrier mobility is up to $\approx 1.2 \times 10^5$ cm^2/V/s [37]. More importantly, the quadratic field dependence of its MR obeys the semiclassical model, representative of conventional (semi)metals.

These observations motivate us to examine in further detail the temperature dependent mean free paths for both momentum relaxing and momentum conserving events, shown in Fig. 5(a). Similar to ZrSiS, the phonon mediated electron-electron mean free path is shorter than the first-order electron-phonon mean free path for all temperature ranges

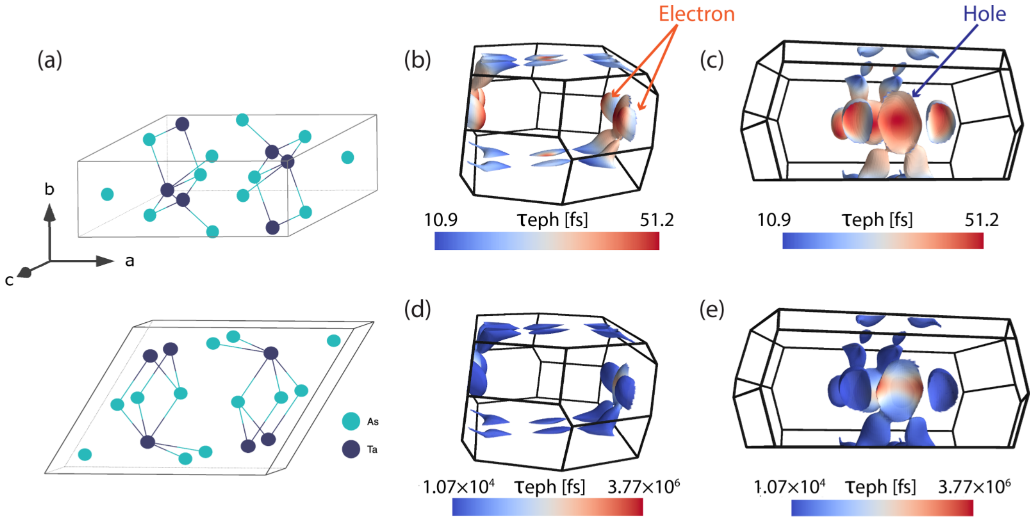

FIG. 4. (a) Crystal lattice of TaAs$_2$, highlighting the monoclinic structure. (b),(c) Electron-phonon lifetimes (τ_{eph}) at 298 K and (d),(e) 4 K projected on the Fermi surface of TaAs$_2$. Different views are presented due to the low symmetry Brillouin zone and the complexity of the electron and hole pockets. The features are highlighted that hole pockets at low temperatures feature much longer momentum relaxing lifetimes.

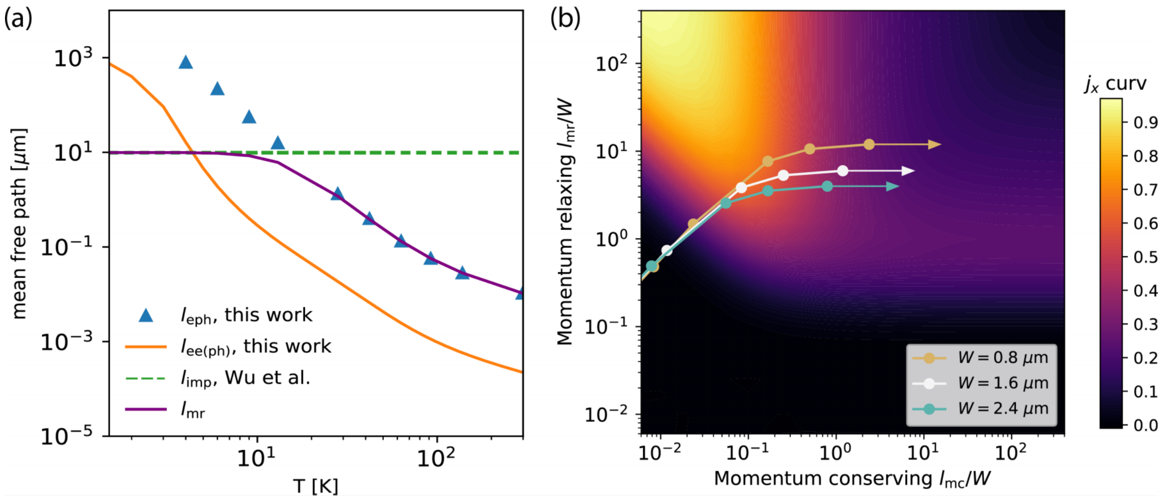

FIG. 5. (a) Temperature dependence of first-order electron-phonon (l_{eph}) and second-order phonon mediated electron-electron ($l_{\mathrm{ee(ph)}}$) mean free paths in TaAs$_2$ calculated from *ab initio*. The impurity mean free path is estimated as 10 μm from earlier works [48,49]. (b) Normalized j_x curvature phase diagram. Overlaid lines show the trajectories with the decreasing temperature with different channel width.

studied. Combined with a long impurity mean free path, this provides a wide temperature window, as well as a wide range of channel widths in which to expect hydrodynamic flow [Fig. 5(b)]. Compared to ZrSiS [Fig. 3(b)] and WTe$_2$ [8], hydrodynamic flow in TaAs$_2$ appears more pronounced, calling for experimental verification.

Investigating the momentum relaxing lifetime distribution on the Fermi surface of TaAs$_2$ [Figs. 4(b)–4(e)], we find similar features to those discussed before. TaAs$_2$ has the valence band maximum located at the L point, while the conduction band minimum is shifted between Γ and L, leading to the coexistence of a few pairs of electron/hole Fermi surfaces located at the boundary of the Brillouin zone. The electron band forms a closed Fermi surface, while the hole band forms an open Fermi surface [48]. At high temperatures, the distribution of τ_{eph} lifetimes is narrow and fairly evenly distributed between the electron and hole pockets. At low temperatures, however, the electron lifetimes are considerably shorter than those of hole carriers, consistent with other semimetals discussed in this work. Despite attempts to classify TaAs$_2$ as a new kind of topological material with $\mathbb{Z}_2$ invariant (0;111) from density functional theory calculations [37], the absence of linear Dirac or Weyl band dispersion indicates that topologically protected band crossings are not a salient ingredient for observing hydrodynamic electron flow. The possibility of observing hydrodynamic flow in TaAs$_2$ is intriguing, suggesting that strong phonon-mediated electron-electron interactions can be found in topologically trivial metals.

IV. ELECTRON-PHONON COUPLING INTERACTIONS AND THE ANALYTICAL LIMITS

Our *ab initio* calculations suggest that, in materials with strong electron-phonon interactions, $l_{\mathrm{mc}} < l_{\mathrm{mr}}$ across all temperatures of interest. In this section, we seek to understand this observation by comparing the second-order phonon-mediated electron-electron interaction analytically to the first-order electron-phonon interaction. To first order in the atomic displacements, the coupled electron-phonon system is described by the Hamiltonian [52]:

$$\hat{H} = \sum_{n\boldsymbol{k}} \epsilon_{n\boldsymbol{k}} \hat{c}^{\dagger}_{n\boldsymbol{k}} \hat{c}_{n\boldsymbol{k}} + \sum_{\boldsymbol{q}\nu} \hbar\omega_{\boldsymbol{q}\nu} (\hat{a}^{\dagger}_{\boldsymbol{q}\nu} \hat{a}_{\boldsymbol{q}\nu} + 1/2) + N^{-1/2} \sum_{\boldsymbol{kq}mn\nu} g_{mn\nu}(\boldsymbol{k},\boldsymbol{q}) \hat{c}^{\dagger}_{m\boldsymbol{k}+\boldsymbol{q}} \hat{c}_{n\boldsymbol{k}} (\hat{a}_{\boldsymbol{q}\nu} + \hat{a}^{\dagger}_{-\boldsymbol{q}\nu}), \tag{2}$$

where $\epsilon_{n\boldsymbol{k}}$ is the single-particle energy for an electron with crystal momentum $\boldsymbol{k}$ in band n, $\omega_{\boldsymbol{q}\nu}$ is the frequency for a phonon with crystal momentum $\boldsymbol{q}$ and polarization ν, $\hat{c}^{\dagger}_{n\boldsymbol{k}}$ and $\hat{c}_{n\boldsymbol{k}}$ ($\hat{a}^{\dagger}_{\boldsymbol{q}\nu}$ and $\hat{a}_{\boldsymbol{q}\nu}$) are the fermionic (bosonic) creation and annihilation operators, respectively, $g_{mn\nu}(\boldsymbol{k},\boldsymbol{q})$ is the matrix element coupling electrons and phonons, and N is the number of unit cells in the phonon supercell.

Using Fermi's golden rule to first and second order, respectively, we can arrive at expressions for the inverse lifetimes of the electronic system due to the coupling with phonons [16]:

$$\frac{1}{\tau^{\mathrm{eph}}_{n\boldsymbol{k}}} = \frac{2\pi}{\hbar} \sum_{m\nu\pm} \int \frac{d\boldsymbol{q}}{\Omega_{\mathrm{BZ}}} \delta(\epsilon_{m\boldsymbol{k}+\boldsymbol{q}} - \epsilon_{n\boldsymbol{k}} \mp \hbar\omega_{\boldsymbol{q}\nu}) \times \left[n_{\boldsymbol{q}\nu} + \frac{1}{2} \mp \left(\frac{1}{2} - f_{m\boldsymbol{k}+\boldsymbol{q}} \right) \right] |g_{mn\nu}(\boldsymbol{k},\boldsymbol{q})|^2, \tag{3}$$

$$\frac{1}{\tau^{\mathrm{ee(ph)}}_{n\boldsymbol{k}}} = \frac{2\pi}{\hbar} \sum_{mpr} \int \frac{d\boldsymbol{q}}{\Omega_{\mathrm{BZ}}} \int \frac{d\boldsymbol{k}'}{\Omega_{\mathrm{BZ}}} |M_{nmpr}(\boldsymbol{k},\boldsymbol{k}',\boldsymbol{q})|^2 \times [f_{p\boldsymbol{k}'} f_{m\boldsymbol{k}+\boldsymbol{q}} + f_{r\boldsymbol{k}'+\boldsymbol{q}}(1 - f_{p\boldsymbol{k}'} - f_{m\boldsymbol{k}+\boldsymbol{q}})] \times \delta(\epsilon_{n\boldsymbol{k}} + \epsilon_{r\boldsymbol{k}'+\boldsymbol{q}} - \epsilon_{p\boldsymbol{k}'} - \epsilon_{m\boldsymbol{k}+\boldsymbol{q}}), \tag{4}$$

where f and n are the Fermi-Dirac and Bose-Einstein equilibrium distribution functions of electrons and phonons, respectively, and Ω_{BZ} is the volume of the first Brillouin zone. Equation (4) can be intuitively thought of as two successive scattering events, whereby an electronic state absorbs an intermediate phonon $|n\boldsymbol{k}\rangle \rightarrow |m(\boldsymbol{k}+\boldsymbol{q})\rangle$, followed by the same intermediate phonon being emitted via electron scattering of $|r(\boldsymbol{k}'+\boldsymbol{q})\rangle \rightarrow |p\boldsymbol{k}'\rangle$. As such, Eqs. (3) and (4) describe the first order electron-phonon ($\tau_{n\boldsymbol{k}}^{\mathrm{e-ph}}$) and second order phonon-mediated electron-electron ($\tau_{n\boldsymbol{k}}^{\mathrm{ee(ph)}}$) interactions, respectively, with

$$M_{nmpr}(\boldsymbol{k},\boldsymbol{k}',\boldsymbol{q}) = \sum_{\nu} \frac{g_{mn\nu}(\boldsymbol{k},\boldsymbol{q})^{*} g_{pr\nu}(\boldsymbol{k}',\boldsymbol{q})}{\hbar\omega_{\boldsymbol{q}\nu} + \epsilon_{n\boldsymbol{k}} - \epsilon_{m\boldsymbol{k}+\boldsymbol{q}} + i\eta}.$$

Diagrammatically, the second order process can be thought of as two $|n\boldsymbol{k}\rangle \rightarrow |m(\boldsymbol{k}+\boldsymbol{q})\rangle$ scattering events, where the momentum exchange occurs by scattering against the same intermediate phonon mode. We note that for processes which go on shell (see Appendix A), the intermediate phonons are real and not necessarily the same, thus allowing for some momentum-relaxing interactions at high temperatures. As such, the momentum conserving scattering rate is given by the contribution of the remaining second order process after the subtraction of first order momentum relaxing processes.

Since we typically only consider interactions near the Fermi level, we introduce Fermi-surface averaged versions of Eqs. (3) and (4) at the Eliashberg level of theory [16,53]:

$$\tau_{\mathrm{eph}}^{-1} = \frac{\pi\beta}{2g(\epsilon_F)} \sum_{\nu} \int \frac{d\boldsymbol{q}}{\Omega_{\mathrm{BZ}}} G_{\boldsymbol{q}\nu} \frac{\omega_{\boldsymbol{q}\nu}}{\sinh^2(\hbar\beta\omega_{\boldsymbol{q}\nu}/2)}, \tag{5}$$

$$\tau_{\mathrm{ee(ph)}}^{-1} = \frac{2\pi}{\hbar g(\epsilon_F)} \sum_{\nu} \int \frac{d\boldsymbol{q}}{\Omega_{\mathrm{BZ}}} G_{\boldsymbol{q}\nu}^{2} \gamma(\hbar\beta\bar{\omega}_{\boldsymbol{q}\nu}). \tag{6}$$

Here, $\beta = 1/k_BT$ is the dimensionless inverse temperature, $g(\epsilon_F)$ is the density of states at the Fermi level per unit cell, and $G_{\boldsymbol{q}\nu}$ is the dimensionless Fermi-surface integrated electron-phonon coupling strength:

$$G_{\boldsymbol{q}\nu} = \sum_{nm} \int \frac{g_s d\boldsymbol{k}}{\Omega_{\mathrm{BZ}}} |g_{mn\nu}(\boldsymbol{k},\boldsymbol{q})|^2 \delta(\epsilon_{n\boldsymbol{k}} - \epsilon_F)\delta(\epsilon_{m\boldsymbol{k}+\boldsymbol{q}} - \epsilon_F) \tag{7}$$

and $\gamma(x)$ is the complex-valued integral, evaluated at the complex phonon frequency (see Appendix A):

$$\gamma(x) \equiv \int_{-\infty}^{\infty} dy \frac{1}{4} \frac{y^2}{\sinh^2(y/2)|x-y|^2},$$
$$\bar{\omega}_{q\nu} = \omega_{q\nu} + i\tau_{q\nu}^{-1}/2 = \omega_{q\nu} + i\pi\omega_{q\nu}G_{q\nu}. \tag{8}$$

Equations (5) and (6) can now directly be compared, by seeking a suitable function approximation to $\gamma(x)$. To this end, we simplify the integrand of Eq. (8) as a power series near $\hbar\beta\omega_{\boldsymbol{q}\nu}$ using a (0,2) Padé approximant, and keep terms to first order in the electron-phonon coupling $G_{\boldsymbol{q}\nu}$ to obtain (see Appendix B)

$$\gamma(\hbar\beta\bar{\omega}_{\boldsymbol{q}\nu}) \approx \frac{\hbar\beta\omega_{q\nu}}{4G_{q\nu}\sinh^2(\hbar\beta\omega_{q\nu}/2)}. \tag{9}$$

Substituting Eq. (9) into Eq. (6), we see that the two rates are identically equal. As such, we conclude that any additional (positive) scattering terms arising from terms higher than linear order in $G_{\boldsymbol{q}\nu}$ can only decrease the phonon-mediated electron-electron lifetime, showing that $\tau_{\mathrm{ee(ph)}}$ is strictly smaller than $\tau_{\mathrm{e-ph}}$.

Equation 9 is most valid for dimensionless electron-phonon couplings $G_{\boldsymbol{q}\nu} \ll 1$, which is true for nonsuperconducting materials systems. Further, the phonon-mediated electron-electron interaction proceeds via the exchange of an "intermediate" phonon, i.e., the phonon emitted (absorbed) by a pair of electrons is assumed to be instantaneously absorbed (emitted) by a different pair of electrons. In practice, this means that other phonon scattering mechanisms, such as anharmonic phonon-phonon scattering, must be "quenched" out, that is, occur at a much slower rate. This assumption is justified at low temperatures, but breaks down at temperatures approaching the material's Debye temperature, and the rate of the first-order process is approaching the second-order process, i.e., $\tau_{\mathrm{eph}}^{-1} \sim \tau_{\mathrm{ee(ph)}}^{-1}$. At those elevated temperatures, one can still use Eq. (B2) by augmenting $G_{\boldsymbol{q}\nu}$ with a competing coupling $G_{\boldsymbol{q}\nu}^{pp}$ capturing anharmonic phonon-phonon interactions. Integrating Eq. (6) numerically using this competing coupling, we find that $\tau_{\mathrm{ee(ph)}}$ naturally increases and can overtake τ_{eph} at high temperatures. In both ZrSiS and TaAs$_2$ (as well as WP$_2$ and WTe$_2$), there is no energy separation between the acoustic branches and the lowest-energy optical modes. These lower-energy optical modes involve large displacements of the heavy Zr/Ta atoms. The heavy transition metal atoms will result in a narrow bandwidth of the acoustic branches and thus a smaller phase space and long phonon-phonon lifetimes, as discussed in high thermal-conductivity system cubic boron arsenide [19].

This analytical limit allows us to revisit and further establish our design principles discussed in Sec. II. To obtain a low enough l_{mc}, we need a material with nonvanishing density of states at the Fermi level, and a large electron-phonon matrix element. While the former observation encourages us to seek for short $\tau_{\mathrm{ee(ph)}}$ in metals, the latter indicates that the electron potential is strongly sensitive to lattice perturbations, i.e., phonons. This is the case when the atomic orbital mixing has low symmetry (i.e., the band extrema are located off high symmetry points in the Brillouin zone), where the electron wave function, or equivalently the charge distribution in real space, is highly anisotropic. To maintain a long enough l_{mr}, large Fermi velocity facilitated by dispersive electronic bands can be combined with long electron-phonon lifetime maintained by reduced electronic phase space at low temperatures. Indeed, the electronic structures of both ZrSiS and TaAs$_2$ explored in this work, as well as WTe$_2$ and WP$_2$ reported earlier, display the above features. There, the Fermi surfaces arise from a combination of d orbitals from the transition metal and p orbitals from the metalloids. These material-specific insights are poised to inform exploration hydrodynamic electron flow in various condensed matter systems.

V. CONCLUSIONS AND OUTLOOK

This article identifies material signatures for hydrodynamic electron flow in semimetals from first principles and predicts two candidates with prominent hydrodynamic effects across a wide temperature range that warrant experimental exploration. We obtain the momentum-relaxing electron-phonon mean free paths l_{mr} and the momentum-conserving phonon mediated electron-electron mean free paths l_{mc} in ZrSiS and TaAs$_2$, and show that the indirect phonon-mediated electron-electron interaction could dominate over a wide temperature range, facilitating hydrodynamic behavior. Through inspection of the momentum relaxing lifetimes on their Fermi surfaces, we find that, at low temperatures, hole pockets with open Fermi surface shape feature much longer lifetimes than electron pockets. These observations suggest that topological Dirac/Weyl bands are not indispensable in the search for promising candidates for hydrodynamic flow, but highly dispersive bands are beneficial in realizing long l_{mr}. We review these signatures in light of previously studied hydrodynamic candidates and discuss the analytical limits of the first- and second-order electron-phonon interactions to find that the mechanism is more broadly applicable. At the Eliashberg level of theory, we then propose general principles for experimental discovery of hydrodynamic behavior in anisotropic metals, such as low symmetry crystals with d/p atomic orbital mixing, suppressed phonon-phonon scattering, and reduced electronic phase space. Future work distinguishing electron-electron Umklapp scattering events and computing the electron viscosity tensor from first principles is still needed to provide a full picture of electron hydrodynamics in quantum materials.

ACKNOWLEDGMENTS

The authors acknowledge fruitful discussions with A. Jermyn, U. Vool, D. Bonn, K. Burch, and A. Yacoby. This work (Y.W., G.V., P.N.) was primarily supported by the Quantum Science Center (QSC), a National Quantum Information Science Research Center of the U.S. Department of Energy (DOE). P.N. acknowledges support as a Moore Inventor Fellow and gratefully acknowledges support through Grant No. GBMF8048 from the Gordon and Betty Moore Foundation. This research used resources of the Oak Ridge Leadership Computing Facility, which is a DOE Office of Science User Facility supported under Contract No. DE-AC05-00OR22725, as well as the resources of the National Energy Research Scientific Computing Center, a DOE Office of Science User Facility supported by the Office of Science of the U.S. Department of Energy under Contract No. DE-AC02-05CH11231.

APPENDIX A: PHONON MEDIATED ELECTRON-ELECTRON SCATTERING

In this Appendix, we derive Eq. (6) starting from Eq. (4). Our starting point for the rate of scattering of an electron in state $|n\boldsymbol{k}\rangle$ via an intermediate phonon is given by Fermi's golden rule by the functional derivative of the transition probability:

$$\begin{aligned}\frac{1}{\tau_{n\boldsymbol{k}}^{\mathrm{ee(ph)}}} &= \frac{2\pi}{\hbar}\sum_{mpr}\int\frac{d\boldsymbol{q}}{\Omega_{\mathrm{BZ}}}\int\frac{d\boldsymbol{k}'}{\Omega_{\mathrm{BZ}}}|M_{nmpr}(\boldsymbol{k},\boldsymbol{k}',\boldsymbol{q})|^2\delta(\epsilon_{n\boldsymbol{k}}+\epsilon_{r\boldsymbol{k}'+\boldsymbol{q}}-\epsilon_{p\boldsymbol{k}'}-\epsilon_{m\boldsymbol{k}+\boldsymbol{q}})\\ &\quad\times\frac{\partial}{\partial f_{n\boldsymbol{k}}}[f_{n\boldsymbol{k}}f_{r\boldsymbol{k}'+\boldsymbol{q}}(1-f_{p\boldsymbol{k}'})(1-f_{m\boldsymbol{k}+\boldsymbol{q}})-(1-f_{n\boldsymbol{k}})(1-f_{e\boldsymbol{k}'+\boldsymbol{q}})f_{p\boldsymbol{k}'}f_{m\boldsymbol{k}+\boldsymbol{q}}]\\ &= \frac{2\pi}{\hbar}\sum_{mpr}\int\frac{d\boldsymbol{q}}{\Omega_{\mathrm{BZ}}}\int\frac{d\boldsymbol{k}'}{\Omega_{\mathrm{BZ}}}|M_{nmpr}(\boldsymbol{k},\boldsymbol{k}',\boldsymbol{q})|^2\delta(\epsilon_{n\boldsymbol{k}}+\epsilon_{r\boldsymbol{k}'+\boldsymbol{q}}-\epsilon_{p\boldsymbol{k}'}-\epsilon_{m\boldsymbol{k}+\boldsymbol{q}})[f_{p\boldsymbol{k}'}f_{m\boldsymbol{k}+\boldsymbol{q}}+f_{r\boldsymbol{k}'+\boldsymbol{q}}(1-f_{p\boldsymbol{k}'}-f_{m\boldsymbol{k}+\boldsymbol{q}})],\end{aligned}\tag{A1}$$

where $M_{nmpr}(\boldsymbol{k},\boldsymbol{k}',\boldsymbol{q})$ is the second-order matrix element defined in Eq. (5).

We define the Fermi-surface averaged scattering rate, by weighing Eq. (A1) with $-\partial_\epsilon f_{n\boldsymbol{k}} = -f'(\epsilon_{n\boldsymbol{k}})$:

$$\begin{aligned}\frac{1}{\tau^{\mathrm{ee(ph)}}} &= \frac{1}{g(\epsilon_F)}\frac{2\pi}{\hbar}\sum_{nmpr}\int\frac{d\boldsymbol{q}}{\Omega_{\mathrm{BZ}}}\int\frac{d\boldsymbol{k}'}{\Omega_{\mathrm{BZ}}}\int\frac{d\boldsymbol{k}}{\Omega_{\mathrm{BZ}}}|M_{nmpr}(\boldsymbol{k},\boldsymbol{k}',\boldsymbol{q})|^2\delta(\epsilon_{n\boldsymbol{k}}+\epsilon_{r\boldsymbol{k}'+\boldsymbol{q}}-\epsilon_{p\boldsymbol{k}'}-\epsilon_{m\boldsymbol{k}+\boldsymbol{q}})\\ &\quad\times[-f'(\epsilon_{n\boldsymbol{k}})][f_{p\boldsymbol{k}'}f_{m\boldsymbol{k}+\boldsymbol{q}}+f_{r\boldsymbol{k}'+\boldsymbol{q}}(1-f_{p\boldsymbol{k}'}-f_{m\boldsymbol{k}+\boldsymbol{q}})]\\ &= \frac{2\pi}{g(\epsilon_F)}\sum_{nmpr}\int\frac{d\boldsymbol{q}}{\Omega_{\mathrm{BZ}}}\int\frac{d\boldsymbol{k}'}{\Omega_{\mathrm{BZ}}}\int\frac{d\boldsymbol{k}}{\Omega_{\mathrm{BZ}}}\int d\omega|M_{nmpr}^{\boldsymbol{k}\boldsymbol{k}'\boldsymbol{q}}(\omega)|^2\delta(\hbar\omega-\epsilon_{m\boldsymbol{k}+\boldsymbol{q}}+\epsilon_{n\boldsymbol{k}})\\ &\quad\times\delta(\epsilon_{n\boldsymbol{k}}+\epsilon_{r\boldsymbol{k}'+\boldsymbol{q}}-\epsilon_{p\boldsymbol{k}'}-\epsilon_{m\boldsymbol{k}+\boldsymbol{q}})[-f'(\epsilon_{n\boldsymbol{k}})][f_{p\boldsymbol{k}'}f_{m\boldsymbol{k}+\boldsymbol{q}}+f_{r\boldsymbol{k}'+\boldsymbol{q}}(1-f_{p\boldsymbol{k}'}-f_{m\boldsymbol{k}+\boldsymbol{q}})],\end{aligned}\tag{A2}$$

where $g(\epsilon_F)$ is the density of states at the Fermi energy per unit cell and we have introduced an auxiliary frequency integral in Eq. (A2) with

$$M_{nmpr}^{\boldsymbol{k}\boldsymbol{k}'\boldsymbol{q}}(\omega) = \sum_\nu\frac{g_{mn\nu}(\boldsymbol{k},\boldsymbol{q})^*g_{pr\nu}(\boldsymbol{k}',\boldsymbol{q})}{\hbar(\omega_{\boldsymbol{q}\nu}-\omega)+i\eta}.\tag{A3}$$

Note that energy conservation and occupation factors ensure all contributing states in Eq. (A2) are near the Fermi level.

To proceed, we assume eigenenergies vary linearly over this energy range and pin $|n\boldsymbol{k}\rangle$ exactly at the Fermi energy. To do this, we must shift the k points of the states involved by splitting the integral over $\boldsymbol{k}$ into two dimensions parallel to the local Fermi surface, and one along the local Fermi velocity (i.e., normal to the Fermi surface), k_v. This is achieved by the following transformations.

(1) Transform $\int dk_v \rightarrow \int dk_v \int dK\,\delta(k_v - K - k_{v0}) \rightarrow \int dk_v'\delta(k_v' - k_{v0})\int dK$, where $k_v' = k_v - K$ is the point pinned to the Fermi surface and K is the distance in k space from that point.

(2) Notice that $\delta(k_v' - k_{v0}) = \delta(\epsilon - \epsilon_F)/|\partial_\epsilon k_v| = \delta(\epsilon - \epsilon_F)|\partial_{kv}\epsilon| = \delta(\epsilon - \epsilon_F)(\hbar v_F)$, and $\int dK = \frac{1}{\hbar v_F}\int de_n$, where we have used $\epsilon(K) = \epsilon_F + \hbar v_F K \equiv \epsilon_F + e_n$ to define e_n as the shifted energy relative to the Fermi level.

(3) Putting these all together, we obtain the substitution $\int dk_v \rightarrow \int dk_v'\delta(\epsilon - \epsilon_F)\int de_n$.

Intuitively, this amounts to pinning $|n\boldsymbol{k}\rangle$ to the Fermi surface using $\delta(\epsilon - \epsilon_F)$ and adding an additional integral over energies e_n which satisfy energy conservation and occupations factors.

Notice that under this transformation $\boldsymbol{k}$ is shifted from its Fermi-surface partner by $\frac{\hat{v}_{n\boldsymbol{k}} e_n}{\hbar v_{n\boldsymbol{k}}}$. Similarly, we can pin $|p\boldsymbol{k}'\rangle$ to the Fermi surface using $\delta(\epsilon_{p\boldsymbol{k}'} - \epsilon_F)$ and an additional integral over e_p, by shifting $\boldsymbol{k}'$ by $\frac{\hat{v}_{p\boldsymbol{k}'} e_p}{\hbar v_{p\boldsymbol{k}'}}$. The transformation for state $|m\boldsymbol{k}+\boldsymbol{q}\rangle$ is achieved by shifting $\boldsymbol{q}$ by $\frac{\hat{v}_{m\boldsymbol{k}+\boldsymbol{q}} e_m}{\hbar v_{m\boldsymbol{k}+\boldsymbol{q}}} - \frac{\hat{v}_{n\boldsymbol{k}} e_n}{\hbar v_{n\boldsymbol{k}}}$. However, since we no longer have a free k-space integral for state $|r\boldsymbol{k}' + \boldsymbol{q}\rangle$, the equivalent shifted k point is instead given by $\boldsymbol{k}_r = \boldsymbol{k}_{r0} + \frac{\hat{v}_{p\boldsymbol{k}'} e_p}{\hbar v_{p\boldsymbol{k}'}} + \frac{\hat{v}_{m\boldsymbol{k}+\boldsymbol{q}} e_m}{\hbar v_{m\boldsymbol{k}+\boldsymbol{q}}} - \frac{\hat{v}_{n\boldsymbol{k}} e_n}{\hbar v_{n\boldsymbol{k}}}$, where $\boldsymbol{k}_{r0}$ is the value that corresponds to the Fermi-surface pinned version of the remaining $\boldsymbol{k}$'s under crystal momentum conservation.

Using these transformations, we can simplify Eq. (A2) to read

$$\begin{aligned}\frac{1}{\tau^{\mathrm{ee(ph)}}} = {} & \frac{2\pi}{g(\epsilon_F)} \sum_{nmpr} \int \frac{d\boldsymbol{q}}{\Omega_{\mathrm{BZ}}} \int \frac{d\boldsymbol{k}'}{\Omega_{\mathrm{BZ}}} \int \frac{d\boldsymbol{k}}{\Omega_{\mathrm{BZ}}} \int d\omega |M_{nmpr}^{\boldsymbol{k}\boldsymbol{k}'\boldsymbol{q}}(\omega)|^2 \delta(\epsilon_{n\boldsymbol{k}} - \epsilon_F)\delta(\epsilon_{p\boldsymbol{k}'} - \epsilon_F)\delta(\epsilon_{m\boldsymbol{k}+\boldsymbol{q}} - \epsilon_F) \int de_r \delta(\epsilon_F + e_r - \epsilon_r) \\ & \times \int de_n \int de_m \int de_p \delta(\hbar\omega + e_n - e_m)\delta(e_n + e_r - e_p - e_m)[-f'(\epsilon_{n\boldsymbol{k}})][f_{p\boldsymbol{k}'} f_{m\boldsymbol{k}+\boldsymbol{q}} + f_{r\boldsymbol{k}'+\boldsymbol{q}}(1 - f_{p\boldsymbol{k}'} - f_{m\boldsymbol{k}+\boldsymbol{q}})],\end{aligned} \tag{A4}$$

where we have defined ϵ_r as the eigenenergy of the state at band r at the shifted $\boldsymbol{k}_r$ and introduced the identity expression $\int de_r \delta(\epsilon_F + e_r - \epsilon_r)$ for convenience in subsequent manipulations.

We proceed by evaluating the innermost three integrals given by the last two lines in Eq. (A4):

$$\begin{aligned} I_3 &= \int de_n \int de_m \int de_p \delta(\hbar\omega + e_n - e_m)\delta(e_n + e_r - e_p - e_m)(-f_n')[f_p f_m + f_r(1 - f_p - f_m)] \\ &= \int de_n \int de_m \int de_p \delta(\hbar\omega + e_n - e_m)\delta(e_n + e_r - e_p - e_m) \frac{\beta e^{\beta e_n}(e^{\beta e_r} + e^{\beta e_m} e^{\beta e_p})}{(e^{\beta e_n} + 1)^2 (e^{\beta e_m} + 1)(e^{\beta e_p} + 1)(e^{\beta e_r} + 1)} \\ &= \int \frac{d\beta e_n}{\beta} \int \frac{d\beta e_m}{\beta} \int \frac{d\beta e_p}{\beta} \frac{\delta(\beta\hbar\omega + \beta e_n - \beta e_m)}{1/\beta} \frac{\delta(\beta e_n + \beta e_r - \beta e_p - \beta e_m)}{1/\beta} \\ &\quad \times \frac{\beta e^{\beta e_m} e^{\beta e_p}}{(e^{\beta e_n} + 1)(e^{\beta e_m} + 1)(e^{\beta e_p} + 1)(e^{\beta e_r} + 1)} \\ &= \int_{-\infty}^{\infty} dx_n \int_{-\infty}^{\infty} dx_m \int_{-\infty}^{\infty} dx_p \frac{\delta(x + x_n - x_m)\delta(x_n + x_r - x_p - x_m) e^{x_m} e^{x_p}}{(e^{x_n} + 1)(e^{x_m} + 1)(e^{x_p} + 1)(e^{x_r} + 1)} \quad (x_i \equiv \beta e_i, x \equiv \beta\hbar\omega) \\ &= \frac{e^{x_r}}{(e^{x_r - x} + 1)(e^{x_r} + 1)} \int_{-\infty}^{\infty} dx_n \frac{e^{x_n}}{(e^{x_n} + 1)(e^x e^{x_n} + 1)} \\ &= \frac{e^{x_r}}{(e^{x_r - x} + 1)(e^{x_r} + 1)} \frac{x}{(e^x - 1)}. \end{aligned} \tag{A5}$$

Note that I_3 decays exponentially as $x_r \to \pm\infty$, and only has significant weight within $x \sim 0$ since

$$\int_{-\infty}^{\infty} dx_r I_3 = \int_{-\infty}^{\infty} dx_r \frac{e^{x_r}}{(e^{x_r - x} + 1)(e^{x_r} + 1)} \frac{x}{(e^x - 1)} = \left(\frac{x}{e^{x/2} - e^{-x/2}}\right)^2 = \mathrm{sinch}^{-2}(x/2). \quad \left(\mathrm{sinch}(x) \equiv \frac{\sinh(x)}{x}\right)$$

As such, we may approximate $I_3 \approx \beta^{-1} \mathrm{sinch}^{-2}(\frac{\beta\hbar\omega}{2})\delta(e_r)$, when $k_B T$ is smaller than the characteristic electronic scale:

$$\begin{aligned} \frac{1}{\tau^{\mathrm{ee(ph)}}} &\approx \frac{2\pi}{g(\epsilon_F)} \sum_{nmpr} \int \frac{d\boldsymbol{q}}{\Omega_{\mathrm{BZ}}} \int \frac{d\boldsymbol{k}'}{\Omega_{\mathrm{BZ}}} \int \frac{d\boldsymbol{k}}{\Omega_{\mathrm{BZ}}} \int d\omega \left|M_{nmpr}^{\boldsymbol{k}\boldsymbol{k}'\boldsymbol{q}}(\omega)\right|^2 \delta(\epsilon_{n\boldsymbol{k}} - \epsilon_F)\delta\big(\epsilon_{p\boldsymbol{k}'} - \epsilon_F\big)\delta(\epsilon_{m\boldsymbol{k}+\boldsymbol{q}} - \epsilon_F) \\ &\quad \times \int de_r \delta(\epsilon_F + e_r - \epsilon_r)\beta^{-1} \mathrm{sinch}^{-2}\left(\frac{\beta\hbar\omega}{2}\right)\delta(e_r) \\ &= \frac{2\pi\beta^{-1}}{g(\epsilon_F)} \sum_{nmpr} \int \frac{d\boldsymbol{q}}{\Omega_{\mathrm{BZ}}} \int \frac{d\boldsymbol{k}'}{\Omega_{\mathrm{BZ}}} \int \frac{d\boldsymbol{k}}{\Omega_{\mathrm{BZ}}} \int d\omega \left|M_{nmpr}^{\boldsymbol{k}\boldsymbol{k}'\boldsymbol{q}}(\omega)\right|^2 \mathrm{sinch}^{-2}\left(\frac{\beta\hbar\omega}{2}\right) \\ &\quad \times \delta(\epsilon_{n\boldsymbol{k}} - \epsilon_F)\delta(\epsilon_{p\boldsymbol{k}'} - \epsilon_F)\delta(\epsilon_{m\boldsymbol{k}+\boldsymbol{q}} - \epsilon_F)\delta(\epsilon_{r\boldsymbol{k}'+\boldsymbol{q}} - \epsilon_F) \end{aligned}$$

$$= \frac{2\pi\beta^{-1}}{g(\epsilon_F)} \int \frac{d\omega}{\mathrm{sinch}^2\left(\frac{\beta\hbar\omega}{2}\right)} \sum_{nmpr} \int \frac{d\boldsymbol{q}}{\Omega_{\mathrm{BZ}}} \int \frac{d\boldsymbol{k}'}{\Omega_{\mathrm{BZ}}} \int \frac{d\boldsymbol{k}}{\Omega_{\mathrm{BZ}}} \left| \sum_{\nu} \frac{g_{mn\nu}(\boldsymbol{k},\boldsymbol{q})^* g_{pr\nu}(\boldsymbol{k}',\boldsymbol{q})}{\hbar(\omega_{\boldsymbol{q}\boldsymbol{\nu}} - \omega) + i\eta} \right|^2$$

$$\times\, \delta(\epsilon_{n\boldsymbol{k}} - \epsilon_F)\delta\big(\epsilon_{p\boldsymbol{k}'} - \epsilon_F\big)\delta(\epsilon_{m\boldsymbol{k}+\boldsymbol{q}} - \epsilon_F)\delta\big(\epsilon_{r\boldsymbol{k}'+\boldsymbol{q}} - \epsilon_F\big). \tag{A6}$$

To simplify further, we introduce the phonon analog of the random phase approximation to move the summation over polarizations outside and split the second order matrix element:

$$\frac{1}{\tau^{\mathrm{ee(ph)}}} = \frac{2\pi\beta^{-1}}{g(\epsilon_F)} \int \frac{d\omega}{\mathrm{sinch}^2\left(\frac{\beta\hbar\omega}{2}\right)} \sum_{\nu nmpr} \int \frac{d\boldsymbol{q}}{\Omega_{\mathrm{BZ}}} \int \frac{d\boldsymbol{k}'}{\Omega_{\mathrm{BZ}}} \int \frac{d\boldsymbol{k}}{\Omega_{\mathrm{BZ}}} \left| \frac{g_{mn\nu}(\boldsymbol{k},\boldsymbol{q})^* g_{pr\nu}(\boldsymbol{k}',\boldsymbol{q})}{\hbar(\omega_{\boldsymbol{q}\boldsymbol{\nu}} - \omega) + i\eta} \right|^2$$

$$\times\, \delta(\epsilon_{n\boldsymbol{k}} - \epsilon_F)\delta\big(\epsilon_{p\boldsymbol{k}'} - \epsilon_F\big)\delta(\epsilon_{m\boldsymbol{k}+\boldsymbol{q}} - \epsilon_F)\delta\big(\epsilon_{r\boldsymbol{k}'+\boldsymbol{q}} - \epsilon_F\big)$$

$$= \frac{2\pi\beta^{-1}}{g(\epsilon_F)} \int \frac{d\omega}{\mathrm{sinch}^2\left(\frac{\beta\hbar\omega}{2}\right)} \sum_{\nu} \int \frac{d\boldsymbol{q}}{\Omega_{\mathrm{BZ}}} \frac{1}{|\hbar(\omega_{\boldsymbol{q}\nu} - \omega) + i\eta|^2} \sum_{nm} \int \frac{d\boldsymbol{k}}{\Omega_{\mathrm{BZ}}} |g_{mn\nu}(\boldsymbol{k},\boldsymbol{q})|^2 \delta(\epsilon_{n\boldsymbol{k}} - \epsilon_F)\delta(\epsilon_{m\boldsymbol{k}+\boldsymbol{q}} - \epsilon_F)$$

$$\times \sum_{pr} \int \frac{d\boldsymbol{k}'}{\Omega_{\mathrm{BZ}}} |g_{pr\nu}(\boldsymbol{k}',\boldsymbol{q})|^2 \delta(\epsilon_{p\boldsymbol{k}'} - \epsilon_F)\delta(\epsilon_{r\boldsymbol{k}'+\boldsymbol{q}} - \epsilon_F)$$

$$= \frac{2\pi\beta^{-1}}{g(\epsilon_F)} \int \frac{d\omega}{\mathrm{sinch}^2\left(\frac{\beta\hbar\omega}{2}\right)} \sum_{\nu} \int \frac{d\boldsymbol{q}}{\Omega_{\mathrm{BZ}}} \frac{G_{\boldsymbol{q}\nu}^2}{|\hbar(\omega_{\boldsymbol{q}\nu} - \omega) + i\eta|^2}, \tag{A7}$$

where $G_{\boldsymbol{q}\nu}$ is the Fermi-surface integrated electron-phonon coupling for each phonon mode, defined in Eq. (7).

In trying to evaluate Eq. (A7), we encounter a $\mathcal{O}(\eta)^{-1}$ singularity when $\omega = \omega_{\boldsymbol{q}\nu}$ (i.e., the intermediate phonon state goes on shell). To account for this, we use the phonon linewidth $\mathrm{Im}\Sigma_{\boldsymbol{q}\nu}$ to construct the complex phonon frequency $\bar{\omega}_{\boldsymbol{q}\nu} = \omega_{\boldsymbol{q}\nu} + (i/\hbar)\mathrm{Im}\Sigma_{\boldsymbol{q}\nu} = \omega_{\boldsymbol{q}\nu} + i\tau_{\boldsymbol{q}\nu}^{-1}/2 = \omega_{\boldsymbol{q}\nu} + i\pi\omega_{\boldsymbol{q}\nu}G_{\boldsymbol{q}\nu}$. Substituting the above complex frequency to Eq. (A7), we arrive at Eq. (6) used in the manuscript.

APPENDIX B: PADÉ APPROXIMANTS

In this Appendix, we expand on the functional approximation, Eq. (9), used in the manuscript starting from Eq. (8):

$$\gamma(x) = \int_{-\infty}^{\infty} dy \frac{1}{4} \frac{y^2}{\sinh^2(y/2)|x-y|^2}. \quad (x = \hbar\beta\bar{\omega}_{\boldsymbol{q}\nu})$$

First, expand the integrand using a (0,2) Padé approximant:

$$\gamma(\hbar\beta\bar{\omega}_{\boldsymbol{q}\nu}) \approx \int_{-\infty}^{\infty} dy(\hbar\beta\omega_{\boldsymbol{q}\nu})^2/\big\{\cosh(\hbar\beta\omega_{\boldsymbol{q}\nu})\big[2y^2 + 6(\pi G_{\boldsymbol{q}\nu}y)^2 + (\pi G_{\boldsymbol{q}\nu}y\hbar\beta\omega_{\boldsymbol{q}\nu})^2$$

$$- 2y\hbar\beta\omega_{\boldsymbol{q}\nu}\big(2 + 8(G_{\boldsymbol{q}\nu}\pi)^2 + (G_{\boldsymbol{q}\nu}\pi\hbar\beta\omega_{\boldsymbol{q}\nu})^2\big) + (\hbar\beta\omega_{\boldsymbol{q}\nu})^2(2 + 12(G_{\boldsymbol{q}\nu}\pi)^2 + (G_{\boldsymbol{q}\nu}\pi\hbar\beta\omega_{\boldsymbol{q}\nu})^2)\big]$$

$$- 2\big(6\pi^2 G_{\boldsymbol{q}\nu}^2 + 1\big)\hbar\beta\omega_{\boldsymbol{q}\nu}^2 - 2\big(3\pi^2 G_{\boldsymbol{q}\nu}^2 + 1\big)y^2 + 4\big(1 + 4\pi^2 G_{\boldsymbol{q}\nu}^2\big)y\hbar\beta\omega_{\boldsymbol{q}\nu}$$

$$- 2\pi^2 G_{\boldsymbol{q}\nu}^2\hbar\beta\omega_{\boldsymbol{q}\nu}(\hbar\beta\omega_{\boldsymbol{q}\nu} - y)(3\hbar\beta\omega_{\boldsymbol{q}\nu} - 2y)\sinh(\hbar\beta\omega_{\boldsymbol{q}\nu})\big\}. \tag{B1}$$

Applying the fundamental theorem of calculus to the antiderivative of Eq. (B1) and simplifying the expression we obtain

$$\gamma(\hbar\beta\bar{\omega}_{\boldsymbol{q}\nu}) \approx \frac{\hbar\beta\omega_{\boldsymbol{q}\nu}}{2G_{\boldsymbol{q}\nu}\sinh^{\frac{3}{2}}\left(\frac{\hbar\beta\omega_{\boldsymbol{q}\nu}}{2}\right)\sqrt{\pi^2 G_{\boldsymbol{q}\nu}^2\left[[(\hbar\beta\omega_{\boldsymbol{q}\nu})^2 + 8]\sinh\left(\frac{\hbar\beta\omega_{\boldsymbol{q}\nu}}{2}\right) - 4\hbar\beta\omega_{\boldsymbol{q}\nu}\cosh\left(\frac{\hbar\beta\omega_{\boldsymbol{q}\nu}}{2}\right)\right] + 4\sinh\left(\frac{\hbar\beta\omega_{\boldsymbol{q}\nu}}{2}\right)}}. \tag{B2}$$

Finally, we simplify the expression under the square root of Eq. (B2) by taking its power series around $G_{\boldsymbol{q}\nu} = 0$ to linear order to obtain Eq. (9):

$$\gamma(\hbar\beta\bar{\omega}_{\boldsymbol{q}\nu}) \approx \frac{\hbar\beta\omega_{\boldsymbol{q}\nu}}{4G_{\boldsymbol{q}\nu}\sinh^2(\hbar\beta\omega_{\boldsymbol{q}\nu}/2)}. \tag{B3}$$

APPENDIX C: MOMENTUM-RELAXING ELECTRON-PHONON SCATTERING

The momentum-relaxing electron scattering rates are evaluated by accounting for the change in momentum between final and initial states based on their relative scattering angle following

$$\left[\tau^{\rm mr}_{\rm eph}(n\mathbf{k})\right]^{-1} = \frac{2\pi}{\hbar}\sum_{m\nu}\int_{\rm BZ}\frac{d\mathbf{q}}{\Omega_{\rm BZ}}|g_{mn,\nu}(\mathbf{k},\mathbf{q})|^2 \times\left[\left(n_{\mathbf{q}\nu}+\frac{1}{2}\mp\frac{1}{2}\right)\delta(\varepsilon_{n\mathbf{k}}\mp\omega_{\mathbf{q}\nu}-\varepsilon_{m\mathbf{k}+\mathbf{q}})\right] \times\left(1-\frac{v_{n\mathbf{k}}\cdot v_{m\mathbf{k}+\mathbf{q}}}{|v_{n\mathbf{k}}||v_{m\mathbf{k}+\mathbf{q}}|}\right), \tag{C1}$$

where $v_{n\mathbf{k}}$ is the group velocity. This is identical to Eq. (3) except for an additional factor accounting for the change in momentum between final and initial states based on their relative scattering angle. We calculate the temperature dependent momentum relaxing $\tau_{\rm mr}$ by taking a Fermi-surface average weighted by $|v_{n\mathbf{k}}|^2$ and the energy derivative of the Fermi occupation for transport properties following

$$\tau^{\rm mr}_{\rm eph} = \frac{\int_{\rm BZ}\frac{d\mathbf{k}}{(2\pi)^3}\sum_n\frac{\partial f_{n\mathbf{k}}}{\partial\varepsilon_{n\mathbf{k}}}|v_{n\mathbf{k}}|^2\tau^{\rm mr}_{\rm eph}(n\mathbf{k})}{\int_{\rm BZ}\frac{d\mathbf{k}}{(2\pi)^3}\sum_n\frac{\partial f_{n\mathbf{k}}}{\partial\varepsilon_{n\mathbf{k}}}|v_{n\mathbf{k}}|^2}. \tag{C2}$$

APPENDIX D: BOLTZMANN TRANSPORT EQUATION

In this Appendix, we briefly outline the framework for calculating the real-space Boltzmann transport equation (BTE) solutions shown in Figs. 5 and 3, following our previous work [8,11]. We solve the electronic Boltzmann transport equation, at the dual-lifetime relaxation time approximation which includes momentum-conserving scattering. At steady state, the evolution of the distribution function $f(\boldsymbol{r},\boldsymbol{k})$ for nonequilibrium electrons in the neighborhood of position $\boldsymbol{r}$ with wave vector $\boldsymbol{k}$ is given by

$$\boldsymbol{v}_{\boldsymbol{k}}\cdot\nabla_{\boldsymbol{r}}f(\boldsymbol{r},\boldsymbol{k})+e\boldsymbol{E}\cdot\nabla_{\boldsymbol{k}}f(\boldsymbol{r},\boldsymbol{k})=\Gamma[f], \tag{D1}$$

where $\boldsymbol{v}_{\boldsymbol{k}}$ is the electron group velocity and $\Gamma[f]$ is the collision integral. We consider flow through a 2D channel $[\boldsymbol{r}=(x,y)]$ of width W, for a spherical Fermi surface $[\boldsymbol{v}=v_{\rm F}(\cos\theta,\sin\theta)]$. Under these approximations, we can linearize (D1) to give an integro-differential equation in terms of an "effective" mean free path, $l_{\rm eff}$ [3,8]:

$$\sin(\theta)\partial_y l_{\rm eff}(y,\theta)+\frac{l_{\rm eff}(y,\theta)}{l}=1+\frac{\tilde{l}_{\rm eff}}{l_{\rm mc}}, \tag{D2}$$

where l is given by Mathhiessen's rule $l^{-1}=l_{mc}^{-1}+l_{mr}^{-1}$. Momentum conservation is accounted for by the last term, which defines the "average" mean free path $\tilde{l}_{\rm eff}(y)$ and is directly proportional to current density, $j_x(y)$:

$$\tilde{l}_{\rm eff}(y)=\int_0^{2\pi}\frac{d\theta}{\pi}\cos^2(\theta)l_{\rm eff}(y,\theta), \tag{D3}$$

$$j_x(y)=\left(\frac{m}{\pi\hbar^2}\right)\varepsilon_{\rm F}e^2\frac{E_x}{mv_{\rm F}}\tilde{l}_{\rm eff}(y), \tag{D4}$$

where m is the electronic effective mass, E_x is the electric field component in the x direction, and v_F is the Fermi velocity. Equation (D2) is solved numerically by transforming it into a Fredholm integral equation of the second kind [3,8]: for each pair of $(l_{\rm mr}/W,\ l_{\rm mc}/W)$ values, solution of Eqs. (D2) to (D4) returns the spatially resolved current density profile $j_x(y)$, from which we extract the scalar-valued current density curvature by fitting a parabola around the center of the channel $y=0$.

[1] D. A. Bandurin, A. V. Shytov, L. S. Levitov, R. K. Kumar, A. I. Berdyugin, M. B. Shalom, I. V. Grigorieva, A. K. Geim, and G. Falkovich, Nat. Commun. **9**, 1 (2018).

[2] V. N. Kotov, B. Uchoa, V. M. Pereira, F. Guinea, and A. H. Castro Neto, Rev. Mod. Phys. **84**, 1067 (2012).

[3] M. J. M. de Jong and L. W. Molenkamp, Phys. Rev. B **51**, 13389 (1995).

[4] D. A. Bandurin, I. Torre, R. K. Kumar, M. B. Shalom, A. Tomadin, A. Principi, G. H. Auton, E. Khestanova, K. S. Novoselov, I. V. Grigorieva, L. A. Ponomarenko, A. K. Geim, and M. Polini, Science **351**, 1055 (2016).

[5] J. Crossno, J. K. Shi, K. Wang, X. Liu, A. Harzheim, A. Lucas, S. Sachdev, P. Kim, T. Taniguchi, K. Watanabe, T. A. Ohki, and K. C. Fong, Science **351**, 1058 (2016).

[6] R. K. Kumar, D. A. Bandurin, F. M. D. Pellegrino, Y. Cao, A. Principi, H. Guo, G. H. Auton, M. B. Shalom, L. A. Ponomarenko, G. Falkovich, K. Watanabe, T. Taniguchi, I. V. Grigorieva, L. S. Levitov, M. Polini, and A. K. Geim, Nat. Phys. **13**, 1182 (2017).

[7] J. Gooth, F. Menges, N. Kumar, V. Suβ, C. Shekhar, Y. Sun, U. Drechsler, R. Zierold, C. Felser, and B. Gotsmann, Nat. Commun. **9**, 4093 (2018).

[8] U. Vool, A. Hamo, G. Varnavides, Y. Wang, T. X. Zhou, N. Kumar, Y. Dovzhenko, Z. Qiu, C. A. Garcia, A. T. Pierce *et al.*, Nat. Phys. **17**, 1216 (2021).

[9] N. Nandi, T. Scaffidi, P. Kushwaha, S. Khim, M. E. Barber, V. Sunko, F. Mazzola, P. D. C. King, H. Rosner, P. J. W. Moll, M. König, J. E. Moore, S. Hartnoll, and A. P. Mackenzie, npj Quantum Mater. **3**, 66 (2018).

[10] P. J. Moll, P. Kushwaha, N. Nandi, B. Schmidt, and A. P. Mackenzie, Science **351**, 1061 (2016).

[11] G. Varnavides, Y. Wang, P. J. Moll, P. Anikeeva, and P. Narang, Phys. Rev. Materials **6**, 045002 (2022).

[12] L. Levitov and G. Falkovich, Nat. Phys. **12**, 672 (2016).

[13] A. Lucas and K. C. Fong, J. Phys.: Condens. Matter **30**, 053001 (2018).

[14] M. J. H. Ku, T. X. Zhou, Q. Li, Y. J. Shin, J. K. Shi, C. Burch, L. E. Anderson, A. T. Pierce, Y. Xie, A. Hamo, U. Vool, H. Zhang, F. Casola, T. Taniguchi, K. Watanabe, M. M. Fogler, P. Kim, A. Yacoby, and R. L. Walsworth, Nature (London) **583**, 537 (2020).

[15] A. Jenkins, S. Baumann, H. Zhou, S. A. Meynell, D. Yang, K. Watanabe, T. Taniguchi, A. Lucas, A. F. Young, and A. C. B. Jayich, arXiv:2002.05065.

[16] J. Coulter, R. Sundararaman, and P. Narang, Phys. Rev. B **98**, 115130 (2018).
[17] G. B. Osterhoudt, Y. Wang, C. A. C. Garcia, V. M. Plisson, J. Gooth, C. Felser, P. Narang, and K. S. Burch, Phys. Rev. X **11**, 011017 (2021).
[18] W. Butler, Phys. Rev. B **15**, 5267 (1977).
[19] L. Lindsay, D. A. Broido, and T. L. Reinecke, Phys. Rev. Lett. **111**, 025901 (2013).
[20] A. H. MacDonald, R. Taylor, and D. J. W. Geldart, Phys. Rev. B **23**, 2718 (1981).
[21] G. F. Giuliani and J. J. Quinn, Phys. Rev. B **26**, 4421 (1982).
[22] M. Kaveh and N. Wiser, Adv. Phys. **33**, 257 (1984).
[23] A. H. Wilson, Proc. R. Soc. London A **167**, 580 (1938).
[24] M. R. van Delft, Y. Wang, C. Putzke, J. Oswald, G. Varnavides, C. A. Garcia, C. Guo, H. Schmid, V. Süss, H. Borrmann *et al.*, Nat. Commun. **12**, 4799 (2021).
[25] N. P. Ong, Phys. Rev. B **43**, 193 (1991).
[26] Y. Wang and P. Narang, Phys. Rev. B **102**, 125122 (2020).
[27] M. N. Ali, J. Xiong, S. Flynn, J. Tao, Q. D. Gibson, L. M. Schoop, T. Liang, N. Haldolaarachchige, M. Hirschberger, N. P. Ong, and R. J. Cava, Nature (London) **514**, 205 (2014).
[28] I. Pletikosić, M. N. Ali, A. V. Fedorov, R. J. Cava, and T. Valla, Phys. Rev. Lett. **113**, 216601 (2014).
[29] N. Kumar, C. Shekhar, S.-C. Wu, I. Leermakers, O. Young, U. Zeitler, B. Yan, and C. Felser, Phys. Rev. B **93**, 241106(R) (2016).
[30] W. Zhou, B. Li, C. Q. Xu, M. R. Delft, Y. G. Chen, X. C. Fan, B. Qian, N. E. Hussey, and X. Xu, Adv. Electron. Mater. **5**, 1900250 (2019).
[31] M. N. Ali, L. M. Schoop, C. Garg, J. M. Lippmann, E. Lara, B. Lotsch, and S. S. P. Parkin, Sci. Adv. **2**, e1601742 (2016).
[32] Y.-Y. Lv, B.-B. Zhang, X. Li, S.-H. Yao, Y. B. Chen, J. Zhou, S.-T. Zhang, M.-H. Lu, and Y.-F. Chen, Appl. Phys. Lett. **108**, 244101 (2016).
[33] Y.-C. Chiu, K.-W. Chen, R. Schönemann, V. L. Quito, S. Sur, Q. Zhou, D. Graf, E. Kampert, T. Förster, K. Yang, G. T. McCandless, J. Y. Chan, R. E. Baumbach, M. D. Johannes, and L. Balicas, Phys. Rev. B **100**, 125112 (2019).
[34] C.-L. Zhang, S.-Y. Xu, I. Belopolski, Z. Yuan, Z. Lin, B. Tong, G. Bian, N. Alidoust, C.-C. Lee, S.-M. Huang, T.-R. Chang, G. Chang, C.-H. Hsu, H.-T. Jeng, M. Neupane, D. S. Sanchez, H. Zheng, J. Wang, H. Lin, C. Zhang *et al.*, Nat. Commun. **7**, 10735 (2016).
[35] F. Arnold, C. Shekhar, S.-C. Wu, Y. Sun, R. D. dos Reis, N. Kumar, M. Naumann, M. O. Ajeesh, M. Schmidt, A. G. Grushin, J. H. Bardarson, M. Baenitz, D. Sokolov, H. Borrmann, M. Nicklas, C. Felser, E. Hassinger, and B. Yan, Nat. Commun. **7**, 11615 (2016).
[36] H. Li, H. He, H.-Z. Lu, H. Zhang, H. Liu, R. Ma, Z. Fan, S.-Q. Shen, and J. Wang, Nat. Commun. **7**, 10301 (2016).
[37] Y. Luo, R. D. McDonald, P. F. S. Rosa, B. Scott, N. Wakeham, N. J. Ghimire, E. D. Bauer, J. D. Thompson, and F. Ronning, Sci. Rep. **6**, 27294 (2016).
[38] M. Diez, A. M. R. V. L. Monteiro, G. Mattoni, E. Cobanera, T. Hyart, E. Mulazimoglu, N. Bovenzi, C. W. J. Beenakker, and A. D. Caviglia, Phys. Rev. Lett. **115**, 016803 (2015).
[39] E. Uykur, L. Z. Maulana, L. M. Schoop, B. V. Lotsch, M. Dressel, and A. V. Pronin, Phys. Rev. Research **1**, 032015(R) (2019).
[40] V. Sunko, P. McGuinness, C. Chang, E. Zhakina, S. Khim, C. Dreyer, M. Konczykowski, H. Borrmann, P. Moll, M. König *et al.*, Phys. Rev. X **10**, 021018 (2020).
[41] I. R. Lapidus, Am. J. Phys. **50**, 45 (1982).
[42] M. Novak, S. N. Zhang, F. Orbanić, N. Biliškov, G. Eguchi, S. Paschen, A. Kimura, X. X. Wang, T. Osada, K. Uchida, M. Sato, Q. S. Wu, O. V. Yazyev, and I. Kokanović, Phys. Rev. B **100**, 085137 (2019).
[43] L. M. Schoop, M. N. Ali, C. Straßer, A. Topp, A. Varykhalov, D. Marchenko, V. Duppel, S. S. P. Parkin, B. V. Lotsch, and C. R. Ast, Nat. Commun. **7**, 11696 (2016).
[44] B.-B. Fu, C.-J. Yi, T.-T. Zhang, M. Caputo, J.-Z. Ma, X. Gao, B. Q. Lv, L.-Y. Kong, Y.-B. Huang, P. Richard, M. Shi, V. N. Strocov, C. Fang, H.-M. Weng, Y.-G. Shi, T. Qian, and H. Ding, Sci. Adv. **5**, eaau6459 (2019).
[45] J. Hu, Z. Tang, J. Liu, Y. Zhu, J. Wei, and Z. Mao, Phys. Rev. B **96**, 045127 (2017).
[46] R. Singha, A. K. Pariari, B. Satpati, and P. Mandal, Proc. Natl. Acad. Sci. USA **114**, 2468 (2017).
[47] M. B. Schilling, L. M. Schoop, B. V. Lotsch, M. Dressel, and A. V. Pronin, Phys. Rev. Lett. **119**, 187401 (2017).
[48] T. A. Butcher, J. Hornung, T. Förster, M. Uhlarz, J. Klotz, I. Sheikin, J. Wosnitza, and D. Kaczorowski, Phys. Rev. B **99**, 245112 (2019).
[49] D. Wu, J. Liao, W. Yi, X. Wang, P. Li, H. Weng, Y. Shi, Y. Li, J. Luo, X. Dai, and Z. Fang, Appl. Phys. Lett. **108**, 042105 (2016).
[50] Y.-Y. Wang, Q.-H. Yu, P.-J. Guo, K. Liu, and T.-L. Xia, Phys. Rev. B **94**, 041103(R) (2016).
[51] Z. Yuan, H. Lu, Y. Liu, J. Wang, and S. Jia, Phys. Rev. B **93**, 184405 (2016).
[52] F. Giustino, Rev. Mod. Phys. **89**, 015003 (2017).
[53] P. B. Allen, Phys. Rev. B **17**, 3725 (1978).